Green Chemistry

PAPER

View Article Online
View Journal | View Issue

Cite this: *Green Chem.*, 2025, **27**, 14595

Perovskite-triggered dual exsolution of oxygen-deficient CeO_2 matrix and NiFe nanoalloys for enhanced CO_2 electrolysis

Biao Ouyang,[a] Ming Yang,[a] Lin-Bo Liu,[a] Shuo Liu,[a] Yan Li,[a] Xian-Zhu Fu,[b] Yifei Sun,[c,d] Subiao Liu *[a] and Jing-Li Luo[b,e]

Perovskite cathodes for CO_2 electrolysis offer excellent redox stability but suffer from limited activity. Although *in situ* exsolution of B-site cations is a powerful strategy to alleviate this issue, this process often triggers co-segregation of insulating AO_x phases, which diminishes active site exposure and ionic-electronic conductivity. Here we addressed the critical issue of insulating phase segregation in conventional exsolved perovskite by developing a Ce-doping strategy in $Sr_{1.95}Ce_{0.05}Fe_{1.3}Ni_{0.2}Mo_{0.5}O_{6-\delta}$ (SCeFNM). This material, upon annealing in a reducing atmosphere, allowed *in situ* construction of nanoscale CeO_2–NiFe/oxide heterostructures (CeO_2–NiFe@SCeFNM) by co-exsolving oxygen-deficient CeO_2 phase and NiFe alloy nanoparticles (NPs) on the surface. The unique architecture achieved a high current density of 1.57 A cm^{-2} at 1.5 V and 850 °C with a CO faradaic efficiency of over 96%, outperforming NiFe@SFNM and their counterparts. Combined results demonstrated that the superior activity mainly came from the synergy within the "three-in-one" heterostructure, where NiFe alloy NPs increased the electronic conductivity, and CeO_2 phase extended the O^{2-} migration channels capable of enhancing CO_2 adsorption and activation, while the perovskite backbone ensured structural integrity. This study establishes a universal paradigm for constructing advanced catalysts for diverse applications *via* co-exsolution of metal NPs and defective oxide phases from appropriately A-site-doped perovskites.

Received 20th August 2025,
Accepted 16th October 2025

DOI: 10.1039/d5gc04390e

rsc.li/greenchem

Green foundation

1. High-temperature CO_2 electrolysis within SOECs has emerged as a transformative pathway, which enables direct conversion of CO_2 into CO or syngas using renewable energy. This study innovatively addresses the critical issue of an insulating SrO phase inherent in conventional exsolution processes by strategically constructing heterostructured CeO_2–NiFe@SCeFNM as a SOEC cathode material, thereby advancing green chemistry and contributing to sustainable technologies.

2. We successfully achieved efficient conversion of CO_2 into industrially vital CO using renewable electricity in an SOEC, which delivered a high current density of 1.57 A cm^{-2} at 850 °C and 1.5 V, together with a high CO faradaic efficiency of over 96%, therefore significantly enhancing carbon utilization efficiency.

3. Future optimization to avoid AO phase segregation of perovskites *via* lowering operating temperatures or substituting rare-earth elements at A-sites could further advance their sustainability and scalable implementation of electrocatalytic carbon-neutral technologies.

1. Introduction

The increasing consumption of fossil fuels has led to significant carbon dioxide (CO_2) emissions, which profoundly impact global warming. An urgency to address climate change, therefore, has propelled CO_2 reduction technologies to the forefront of sustainable energy research, offering a dual solution for CO_2 utilization and renewable energy storage.[1,2] Among them, high-temperature CO_2 electrolysis within solid oxide electrolysis cells (SOECs) has emerged as a promising technology, enabling direct conversion of CO_2 into CO or syngas using renewable energy.[3,4] Despite the remarkable catalytic perform-

[a]*School of Minerals Processing and Bioengineering, Central South University, Changsha, Hunan 410083, China. E-mail: subiao@csu.edu.cn; Tel: +86 15675160502*
[b]*College of Materials Science and Engineering, Shenzhen University, Shenzhen 518055, China*
[c]*College of Energy, Xiamen University, Xiamen 361005, China*
[d]*Shenzhen Research Institute of Xiamen University, Shenzhen 518000, China*
[e]*Department of Chemical and Materials Engineering, University of Alberta, Edmonton, Alberta T6G 1H9, Canada*

ance of Ni-yttrium stabilized zirconia (Ni-YSZ) cermet as an SOEC cathode, it suffers from intrinsic redox instability, agglomeration and severe coking issues, which critically limit its further utilization at larger industrial-scale application.[5–7] Alternatively, perovskite oxides (*e.g.*, ABO_3, A_2BO_4) have been extensively investigated as promising catalysts for SOECs due to their mixed ionic-electronic conductivity and superior redox stability.[8,9] Nevertheless, a major limitation lies in their relatively inferior catalytic activity, which leads to an insufficient electrolysis performance, highlighting the imperativeness of exploring smart design strategies for perovskite oxide electrodes.

Surface engineering *via in situ* exsolution has emerged as a powerful strategy to enhance catalytic activity by enabling controlled growth of nanoscale metallic nanoparticles (NPs) on perovskite oxide surfaces.[4,10–12] This strategy not only achieves a uniform dispersion of catalytic NPs across porous electrode architectures, but also generates abundant oxygen vacancies at the metal–oxide interfaces, thereby creating additional electrochemically active sites that improve CO_2 adsorption and activation capabilities. Furthermore, it ensures a high operational stability by mitigating active site loss caused by catalyst detachment and/or agglomeration, while maintaining structural integrity under harsh operating conditions.[13] Among various metal NPs (*e.g.*, Fe, Co, Ni, and Cu), *in situ* exsolution of Fe-/Ni-based metals/alloys has been widely employed since Fe shows exceptional CO_2 adsorption capacity and coking resistance, while Ni demonstrates a superior catalytic activity with the lowest activation energy barrier.[12,14] However, the exsolution of B-site reducible cations may induce the intergrowth of AO_x phases, which alters the functional properties of the material.[11,15] Previous studies have demonstrated that exsolution of B-site cations from perovskite oxides triggers SrO co-segregation on occasion—a process driving chronic electrochemical performance decay since the electronically and ionically insulating nature of surface-terminated SrO obstructs surface charge transfer and oxygen transport pathways.[16,17] Moreover, in cation-ordered $LnBaCo_2O_{5+\delta}$ perovskites (Ln = lanthanide), BaO segregation is also kinetically accelerated at temperatures exceeding 400 °C, resulting in a diminished surface coverage of Co active sites on the perovskite oxide framework.[18]

However, it is worth noting that the exsolution of A-site oxides is not always detrimental, since precise design of A-site oxide exsolution offers unprecedented opportunities to tailor CO_2 adsorption and oxygen exchange reactions, which serves as an alternative approach to enhancing SOEC performance. For instance, the exsolution of CaO and NiFe NPs from $La_{0.6}Ca_{0.4}Fe_{0.8}Ni_{0.2}O_{3-\delta}$ doubled its specific surface area.[19] Likewise, Zhu *et al.* synthesized self-generated Fe/MnO_x NPs by regulating A-site deficiency, and the interfacial charge redistribution of Fe/MnO_x optimized CO_2 dissociation pathways and promoted chemical adsorption and dissociation of CO_2 molecules on the cathode surface.[20] Moreover, the exsolution of oxides can also increase oxygen vacancy content and boost O^{2-} migration. Previous studies have reported that Bi-doped $La_{0.4}Sr_{0.6}Co_{0.2}Fe_{0.7}Nb_{0.1}O_{3-\delta}$ exsolved Bi_2O_3 and CoFe alloy NPs, which raised the oxygen vacancy concentration by 40%,[21] while oxygen vacancy-enriched PrO_x NPs enhanced O^{2-} migration capability, which accelerated O^{2-} exchange and migration processes on the electrode surface.[22] Therefore, precise engineering of oxide-metal/oxide heterointerfaces holds the potential to enhance CO_2 electrolysis activity and stability. Cerium oxide (CeO_2), due to its exceptional oxygen storage capacity and redox cycling between Ce^{3+} and Ce^{4+}, possesses a desirable level of O^{2-} conductivity, and the redox couple of $Ce^{4+/3+}$ on the surface accelerates O^{2-} transfer between CO_2 and CO. Meanwhile, NiFe alloy NPs, characterized by their high electronic conductivity and robust thermal stability, are promising candidates for CO_2 dissociation and CO desorption. However, individual NiFe alloy NPs suffer from insufficient O^{2-} migration, while pure CeO_2 lacks the electronic conductivity required for efficient charge transfer in CO_2 electrolysis.

Recognizing this complementary potential between CeO_2 and NiFe alloy NPs, herein we designed and synthesized a novel Ce-doped heterostructured catalyst by annealing $Sr_{1.95}Ce_{0.05}Fe_{1.3}Ni_{0.2}Mo_{0.5}O_{6-\delta}$ (SCeFNM) in a reducing atmosphere to strategically construct metallic NPs with oxygen-vacancy-rich CeO_2 on SCeFNM (CeO_2–NiFe@SCeFNM), realizing dual exsolution of NiFe alloy and CeO_2 NPs with enhanced electronic conductivity, O^{2-} migration, and CO_2 adsorption and activation. Experimental results demonstrated that a cell with a CeO_2–NiFe@SCeFNM cathode achieved a comparable current density (j) of 1.57 A cm^{-2} at 850 °C and 1.5 V for pure CO_2 atmosphere, together with a high CO faradaic efficiency (FE_{CO}) of over 96% and a stability of more than 120 hours, showcasing an exceptional catalytic activity for CO_2 electrolysis. The strategic integration of dual phases through doping-induced co-precipitation offers a compelling approach to synergizing their complementary functionalities.

2. Experimental methods

2.1 Material synthesis

$Sr_2Fe_{1.3}Ni_{0.2}Mo_{0.5}O_{6-\delta}$ (SFNM), SCeFNM, and $La_{0.4}Ce_{0.6}O_2$ (LDC) were obtained *via* a sol–gel method.[23] Stoichiometric amounts of $Sr(NO_3)_2$, $Fe(NO_3)_3{\cdot}9H_2O$, $Ni(NO_3)_3{\cdot}6H_2O$, $(NH_4)_6Mo_7O_{24}{\cdot}4H_2O$ and $Ce(NO_3)_3{\cdot}6H_2O$ were dissolved in EDTA-$NH_3{\cdot}H_2O$ combined solution under continuous heating and stirring; citric acid was then introduced into the solution. The molar ratio of EDTA : citric acid : total cation was controlled to be around 1 : 1.5 : 1. Subsequently, $NH_3{\cdot}H_2O$ was added to adjust the pH value to around 8. The solution was stirred and heated on a hot plate at 80 °C until the formation of organic resins containing homogeneously distributed cations because of the slow evaporation of the solvent. The formed gels were heated at 300 °C for four hours to remove the organic components and the nitrates, followed by being annealed at 1100 °C for 10 hours to achieve the target powders. NiFe@SFNM and CeO_2-NiFe@SCeFNM were pre-

pared by annealing SFNM and SCeFNM powders at 850 °C for 2 hours in a 5% H_2/Ar atmosphere with a flow rate of 50 mL min^{-1} in a tubular furnace. The heating and cooling rates were both controlled at 2 °C min^{-1}. The $La_{0.8}Sr_{0.2}Ga_{0.8}Mg_{0.2}O_{3-\delta}$ (LSGM) electrolyte was prepared by a dry-press method, and then calcined at 1450 °C for 5 hours. The $(La_{0.6}Sr_{0.4})_{0.95}Co_{0.2}Fe_{0.8}O_{3-\delta}$ (LSCF) and $Ga_{0.2}Ce_{0.8}O_{2-\delta}$ (GDC) powders were used as received.

2.2 Material characterization

The crystalline structure of all the synthesized powders was identified by X-ray diffraction (XRD) with Rigaku Rota flex Cu Kα radiation (40 kV, 44 mA), and the raw data were analyzed with JADE version 6.5. Microstructures were determined with a high-resolution Zeiss Sigma field emission scanning electron microscope (SEM). The low- and high-resolution transmission electron microscopy (TEM) images were acquired by using a Thermo Scientific Talos F200X STEM at an accelerating voltage of 200/300 kV. Energy-dispersive X-ray spectroscopy (EDX) combined with high-resolution TEM (HR-TEM) was applied to characterize the composition and element distribution. X-ray photoelectron spectroscopy (XPS, Kratos AXIS Ultra) was used to investigate the surface chemistry of SFNM, SCeFNM, and CeO_2–NiFe@SCeFNM with adventitious carbon (C 1s) at a binding energy (BE) of 284.8 eV as the reference. Temperature-programmed desorption of CO_2 (CO_2-TPD) was investigated with a Micromeritics chemisorption analyzer (Auto Chem II 2920) to study the CO_2 desorption. The CO_2 adsorption ability was also characterized by Fourier transform infrared (FTIR) spectroscopy (Nicolet iS50). The oxygen vacancy content was measured using an iodometric titration method under Ar atmosphere.

2.3 Cell fabrication and measurement

The LDC buffer layer was formed by screen-printing an α-terpinol/ethyl cellulose-bound slurry onto LSGM followed by 1350 °C calcination for 2 hours. Subsequently, CeO_2–NiFe@SCeFNM-GDC, NiFe@SFNM-GDC, SCeFNM-GDC, SFNM, and LSCF-GDC powders were separately mixed with a binder composed of α-terpinol and ethyl cellulose ether to form their corresponding slurries. GDC was incorporated into all cathodes primarily to enhance the oxygen-ion conductivity and extend the triple-phase boundaries. The electrode slurry was screen printed on the LSGM electrolyte, followed by calcining at 1100 °C for 2 hours, to obtain a cell configuration of CeO_2–NiFe@SCeFNM-GDC‖LDC‖LSGM‖LSCF-GDC. The effective area of the electrode was 0.5 cm^2 and Ag paste was used as the current collector. The as-fabricated single cell was mounted on one end of an alumina support for electrochemical measurements, with the LSCF-GDC anode exposed to ambient air. Before testing, the CeO_2–NiFe@SCeFNM cathode compartment was purged with 5% H_2/Ar. Then, pure CO_2 was fed to the cathode at a flow rate of 50 mL min^{-1} for testing. A schematic diagram of the high-temperature CO_2 electrolysis setup is shown in Fig. S1. The electrochemical performance of the single cell was evaluated using an EnergyLab XM electrochemical workstation from OCV to 1.6 V at a scan rate of 20 mV s^{-1}. Electrochemical impedance spectra (EIS) were acquired with an applied AC amplitude of 10 mV in the frequency range of 0.1 Hz to 1.0 MHz. The CO_2 and CO contents of outlet gas were determined by online gas chromatography (Agilent 8860) using a thermal conductivity detector.

3. Results and discussion

The pristine perovskite oxides, SFNM and SCeFNM, were synthesized using a facile sol–gel method, as reported elsewhere.[24,25] The XRD patterns of SFNM and SCeFNM powders after calcination at 1100 °C were detected without impure phase (Fig. S2), but slight shifts of all diffraction peaks toward higher angles were observed for SCeFNM, indicating lattice volume shrinkage due to the partial substitution of a smaller ionic radius of Ce^{3+} (1.14 Å) to Sr^{2+} (1.34 Å). After annealing SFNM and SCeFNM powders at 850 °C in 5% H_2/Ar for 2 hours, the double perovskite oxide phase of SCeFNM was transformed into a Ruddlesden–Popper phase (Fig. 1a), together with dual exsolutions of A-site CeO_2 phase and B-site NiFe alloy NPs (CeO_2–NiFe@SCeFNM). In contrast, only NiFe alloy NPs were *in situ* exsolved from SFNM (NiFe@SFNM), accompanied with a slight phase transformation. To gain insights into the microstructural features, SFNM, SCeFNM, NiFe@SFNM, and CeO_2–NiFe@SCeFNM powders were subjected to SEM analysis. It was seen that SFNM and SCeFNM specimens showed smooth network structures (Fig. S3) whereas substantial NiFe alloy NPs appeared on the reduced SFNM and SCeFNM. Different from NiFe@SFNM, SCeFNM with Ce doping possessed a greater amount of exsolved NiFe alloy NPs, alongside a minor quantity of CeO_2 NPs (Fig. 1b). For further confirmation, HR-TEM was conducted, and it was found that lattice spacings of 0.202 and 0.313 nm were observed in HR-TEM images (Fig. 1c–d and S4) which corresponded to the (111) planes of CeO_2 and NiFe alloy, respectively. Accordingly, the high-angle annular dark-field scanning TEM (HADDF-STEM) image and EDX elemental mapping of CeO_2–NiFe@SCeFNM (Fig. 1e and f) demonstrated that the perovskite oxide surface was uniformly dispersed with CeO_2 and abundant NiFe alloy NPs with an average size of 17.5 ± 3.2 nm, while other elements (*e.g.*, Sr, Mo, O) were homogeneously distributed within the perovskite oxide matrix. Moreover, the exsolved NPs were firmly embedded on the CeO_2–NiFe@SCeFNM substrate, indicating the presence of strong oxide-metal/oxide interactions at the heterointerfaces.

Surface chemical variation of the as-synthesized perovskite oxides was characterized *via* XPS. The XPS full survey spectrum exhibited a Ce element signal in the CeO_2–NiFe@SCeFNM sample, further confirming the presence of Ce^{4+} (Fig. S5). Clearly, Fig. 2a and b showed that an increase in A-site Ce-doping led to a decrease in the intensities of Fe^{3+} and Ni^{3+} species instead of an increase in those of Fe^{2+} and Ni^{2+} species. This implied that increasing A-site Ce-doping reduced the oxidation states of Fe and Ni, and caused an enhanced

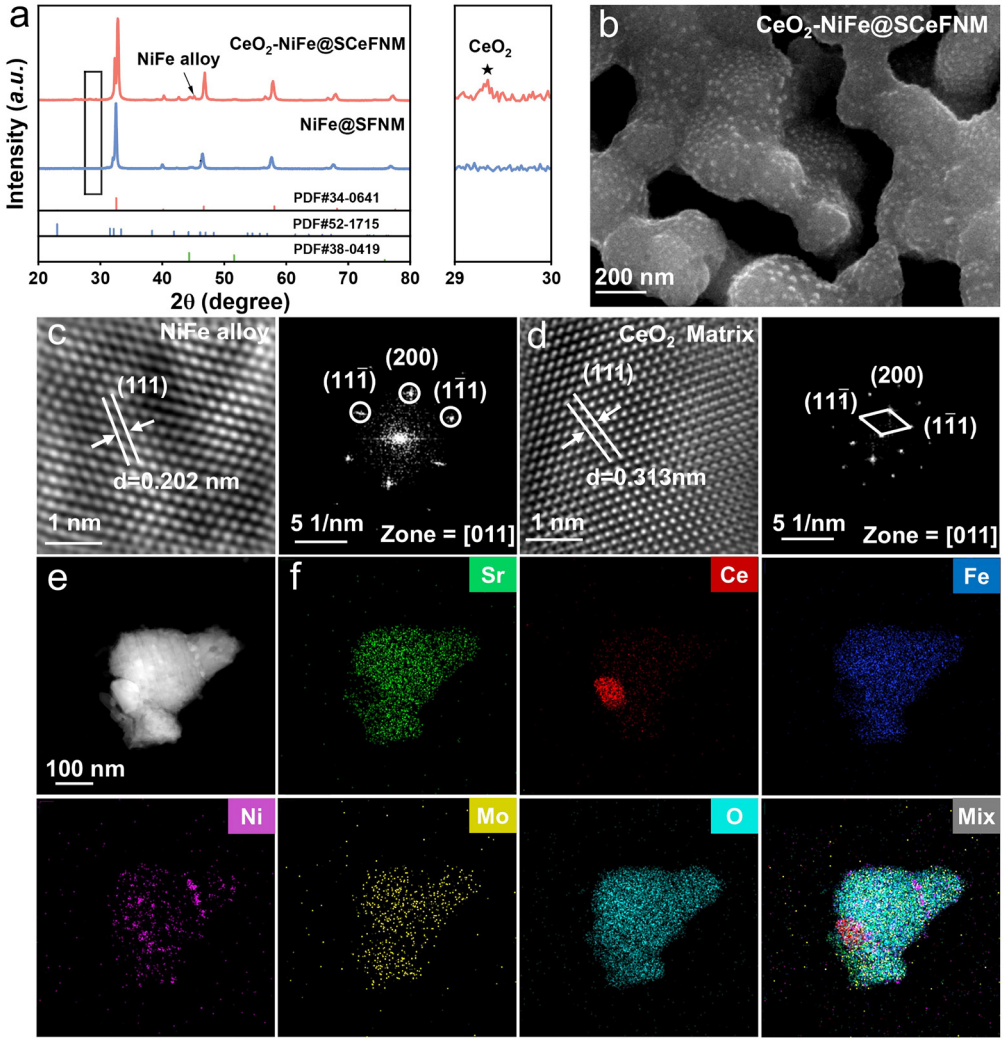

Fig. 1 (a) XRD patterns of NiFe@SFNM and CeO_2–NiFe@SCeFNM, together with an enlargement of the region at 29–30°. (b) SEM image of CeO_2–NiFe@SCeFNM. HR-TEM images and corresponding FFT patterns of (c) NiFe NPs and (d) CeO_2 NPs. (e) HADDF-STEM image of CeO_2–NiFe@SCeFNM with (f) EDX mappings of all elements.

electronegativity, which induced the formation of more oxygen vacancies in turn to maintain the charge neutrality. Notably, two additional peaks at 707 and 852 eV were observed for CeO_2–NiFe@SCeFNM, which were ascribed to the presence of Fe^0 and Ni^0. Moreover, the O 1s spectra were deconvoluted into three subpeaks, representing the lattice oxygen (O_{Latt}), the adsorption oxygen (O_{Ads}), and the surface carbonate/hydroxyl oxygen (CO_3^{2-}/OH^-) species, respectively.[26] Typically, the peak of O_{Ads} represented oxygen vacancies, and it is worth noting that CeO_2–NiFe@SCeFNM demonstrated a higher concentration of O_{Ads} as compared with SFNM and SCeFNM (Fig. 2c), confirming its oxygen vacancy concentration had a considerable enhancement, which aligned well with the iodine titration results in Fig. 2d, confirming its superiority for CO_2 adsorption. To examine the impact of oxygen vacancies on CO_2, its adsorption behaviors on SFNM, SCeFNM, and CeO_2–NiFe@SCeFNM powders were explored in the temperature range of 50–850 °C using CO_2-TPD. There were no desorption peaks observed at low temperatures (<300 °C) in Fig. 2e, while the peaks in the high-temperature range (>300 °C) were mainly associated with the desorption of chemisorbed CO_2.[27] Clearly, the peak area for CeO_2–NiFe@SCeFNM, benefitting from the exsolved CeO_2 phase with abundant oxygen vacancies, was significantly larger than those for SFNM and SCeFNM, indicative of a superior CO_2 adsorption capacity.[28] The elevated desorption temperature of 754 °C indicated an improved bonding ability between CO_2 molecules and perovskite oxides,[16] which coincided well with the working temperatures of SOECs. Furthermore, since carbonates are critical intermediate species in the CO_2 electrolysis process,[29] CO_2 chemisorption was further characterized by FTIR spectroscopy with samples being exposed to CO_2 at 800 °C for 10 hours. As shown in Fig. 2f, the CO_3^{2-} absorption signals in the infrared region of ~1440 cm^{-1} for CeO_2–NiFe@SCeFNM were stronger

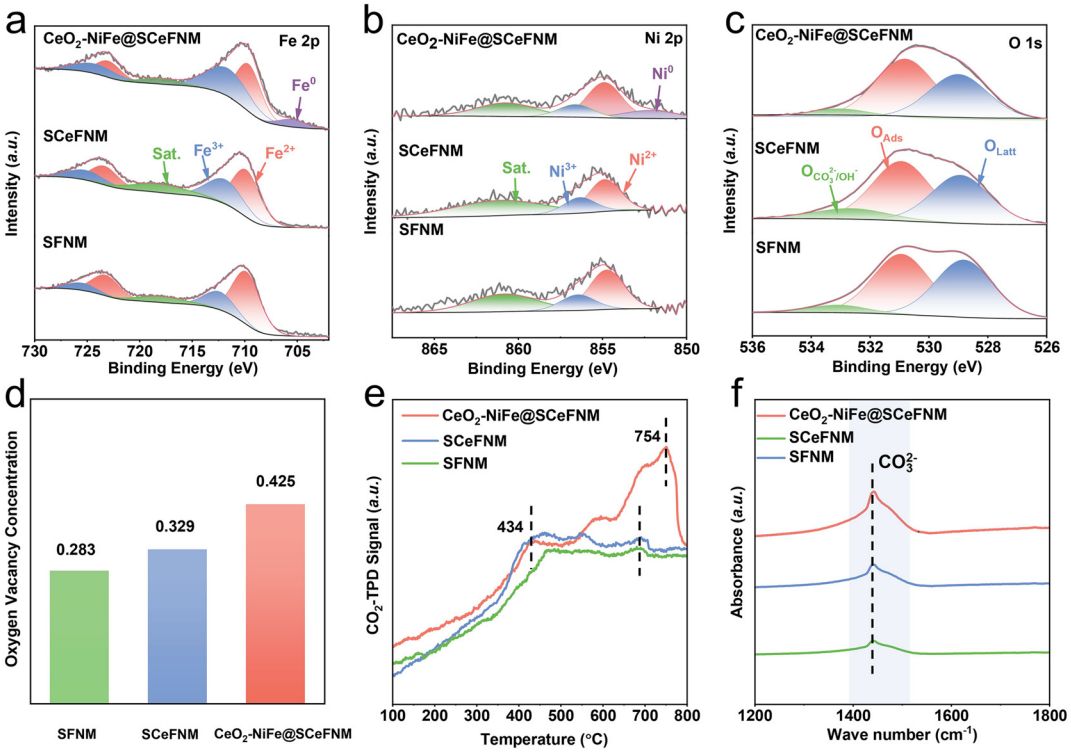

Fig. 2 (a) Fe 2p spectra, (b) Ni 2p spectra, (c) O 1s spectra, (d) oxygen vacancy concentration determined by iodometric titration, (e) CO_2-TPD plots and (f) FTIR spectra of SFNM, SCeFNM, NiFe@SFNM and CeO_2–NiFe@SCeFNM.

as compared to SFNM and SCeFNM, confirming that CeO_2–NiFe@SCeFNM could significantly enhance CO_2 adsorption capacity attributed to the greater amount of oxygen vacancies.[30] In particular, *in situ* FTIR spectra for CeO_2–NiFe@SCeFNM all presented strong CO_3^{2-} signals from 750 to 850 °C (Fig. S6), demonstrating its robust CO_2 adsorption capability.

To unravel the impacts of exsolved CeO_2 phase and NiFe alloy NPs as well as their constructed oxide-metal/oxide heterointerface on CO_2 electrolysis activity, SFNM, SCeFNM, NiFe@SFNM, and CeO_2–NiFe@SCeFNM were fabricated as cathodes within SOECs supported by LSGM electrolyte, and were tested in pure CO_2 atmosphere from 750 to 850 °C. Based on the current–voltage (*I*–*V*) curves, a gradual increase in *j* was observed for all the samples with an order of SFNM < SCeFNM < NiFe@SFNM < CeO_2–NiFe@SCeFNM (Fig. 3a and S7), delivering a *j* of 1.57, 1.45, 1.35 and 1.23 A cm^{-2} at 1.5 V and 850 °C, respectively (Table S1). This implied that as compared to conventional SFNM with only NiFe alloy NPs and pristine SFNM, CeO_2–NiFe@SCeFNM provided more reactive centers precisely due to the dual exsolution of precipitated CeO_2 and NiFe NPs, both of which synergistically facilitated the activity. Concurrently, the key reaction steps and kinetic behaviors during CO_2 electrolysis were investigated using EIS (Fig. S8) and the distribution of relaxation times (DRT) (Fig. S9). The Nyquist plots in Fig. 3b illustrate that the polarization resistance (R_p) values of SFNM, SCeFNM, NiFe@SFNM, and CeO_2–NiFe@SCeFNM cathodes under open-circuit voltage (OCV) at 850 °C were 1.025, 0.885, 0.857, and 0.792 Ω cm^2, respectively, in accordance with the *j* variation trend. Given that the contributions from the LSCF anode and LSGM electrolyte to the total resistance were quite close for all cells, the polarization resistance discrepancy stemmed from the different cathodes. Based on previous studies involving DRT analysis it was known that the peaks at low, intermediate, and high frequency (LF, IF, and HF) are associated with CO_2 adsorption and activation, migration of O^{2-} in the electrodes, and charge/ion transfer at the electrode–electrolyte interface, respectively.[13,31] Apparently, the dual exsolution treatment reduced the LF region area while leaving the IF and HF regions unaffected (Fig. 3c), suggesting that the diminished LF contribution for the CeO_2–NiFe@SCeFNM cathode optimized the CO_2 adsorption and activation kinetics. Furthermore, the R_p value of CeO_2–NiFe@SCeFNM decreased markedly with increasing applied potential (Fig. S8a and Table S2), reflecting an accelerated CO_2 electrolysis kinetics under high potentials. Moreover, increasing the applied potential could lower the LF region area, thus improving CO_2 adsorption and activation, and the ultimate CO_2 electrolysis activity (Fig. S9a). In contrast, raising the operating temperature lowered both the ohmic resistance (R_o) and R_p (Fig. S8e and Table S3), and the accordingly reduced IF and LF region areas in DRT plots revealed that the increase in temperature not only enhanced CO_2 adsorption and activation, but also accelerated O^{2-} migration at the electrode (Fig. S9e).[32]

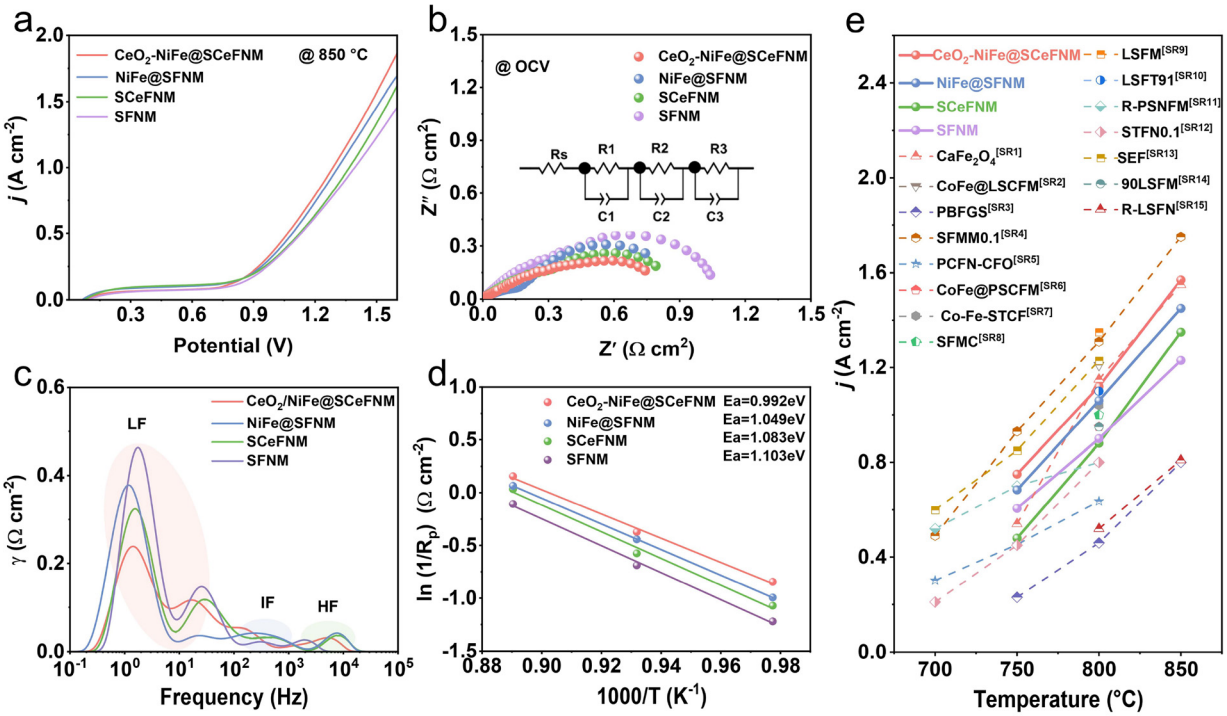

Fig. 3 (a) *I–V* curves, (b) Nyquist plots and (c) DRT results of SFNM, SCeFNM, NiFe@SFNM and CeO_2–NiFe@SCeFNM at 850 °C. (d) Arrhenius plots of various cathodes from 750 to 850 °C. (e) Activity comparison of all samples in this study with previously reported state-of-the-art materials for CO_2 electrolysis at 1.5 V, where SR represents the reference in SI.

This was further verified by the electrochemical activation energy, an important parameter to assess the CO_2 electrolytic process. The Arrhenius plots in Fig. 3d show that the CeO_2–NiFe@SCeFNM cathode delivered a smaller activation energy of 0.992 eV than its counterparts, indicative of a reduced cathodic energy barrier. As a result, benefiting from the synergy of NiFe alloy NPs and CeO_2 phase, CeO_2–NiFe@SCeFNM achieved the optimal CO_2 electrolysis performance among all the control materials, and surpassed that of most of the state-of-the-art cathode materials reported to date, as shown in Fig. 3e, again confirming its superiority for CO_2 electrolysis in SOECs.

As crucial parameters to evaluate CO_2 conversion efficiency, CO production rate (PR_{CO}) and FE_{CO} are equally important for the development of SOECs. The potentiostatic CO_2 electrolysis measurements at varying applied potentials revealed that CeO_2–NiFe@SCeFNM achieved maximum j in a wide potential range from 1.0 to 1.5 V (Fig. 4a), which matched well with the *I–V* results. Additionally, the corresponding FE_{CO} and PR_{CO} under different applied potentials at 850 °C were also evaluated (Fig. 4b). The single cell with the CeO_2–NiFe@SCeFNM cathode achieved a high FE_{CO} of 96.03%, surpassing the 90.94% on SFNM and closely matching those of 95.72% on NiFe@SFNM and 95.35% on SCeFNM in CO_2-to-CO conversion, at 1.5 V and 850 °C. In addition, at 1.5 V, the PR_{CO} of CeO_2–NiFe@SCeFNM reached 10.32 mL min^{-1} cm^{-2}, faster than those of 9.68, 8.68 and 8.42 mL min^{-1} cm^{-2} over NiFe@SFNM, SCeFNM, and SFNM, respectively, which further confirmed that except for j, co-exsolution of CeO_2 phase and NiFe alloy NPs also improved CO_2 conversion rate. The long-term stabilities of the cells with different cathodes were also investigated, and Fig. 4c shows j and FE_{CO} as a function of time under a constant potential of 1.2 V at 850 °C. The CeO_2–NiFe@SCeFNM-assembled cell could maintain a good performance with a negligible j decay rate of 0.793 mA h^{-1} during continuous operation of 120 hours, and retained a steady FE_{CO} of 90%, superior to that of the cells with NiFe@SFNM, SCeFNM, and SFNM. For a better holistic view, a radar map presenting j (A cm^{-2}), $1/R_p$ (Ω^{-1} cm^{-2}), PR_{CO} (mL min^{-1} cm^{-2}), FE_{CO} and stability retention rate per 100 hours ($R_{sr} = j_{100}/j_{initial}$)[25] is plotted in Fig. 4d for comparison. It illustrated clearly that dual exsolution was more beneficial for CO_2 electrolysis, which also highlighted the critical role of CeO_2 phase in tuning CO_2 electrolysis activity. In addition, no extra phase and impurity were observed in the XRD pattern post-test for the CeO_2–NiFe@SCeFNM cathode (Fig. 4e), indicating a good structural stability under harsh electrolysis conditions. Meanwhile, the cathode-electrolyte interface remained closely stacked, and no delamination was detected after long-term CO_2 electrolysis operation (Fig. 4f and S10a, b). Importantly, the perovskite oxide matrix still retained the uniformly anchored *in situ* exsolved NPs without severe agglomeration for the CeO_2–NiFe@SCeFNM cathode (Fig. 4g). However, there were no noticeable *in situ* exsolved NPs on the NiFe@SFNM cathode (Fig. S10c), clarifying a good structural resilience under high-temperature harsh conditions in the mixture of

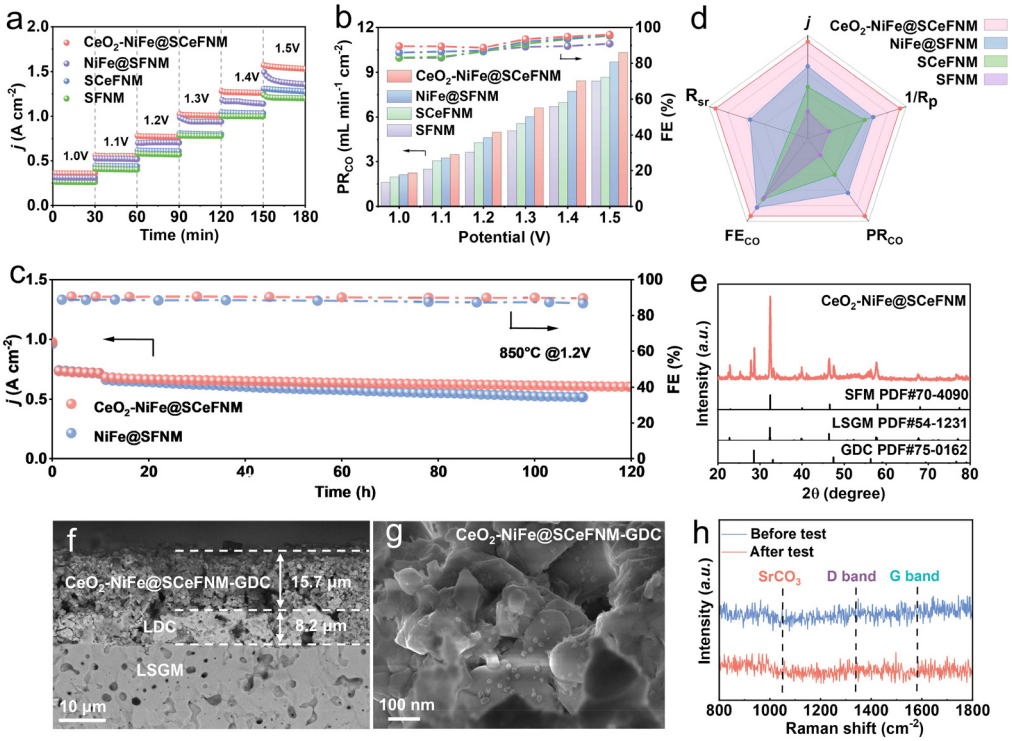

Fig. 4 (a) The potentiostatic measurements for CO_2 electrolysis and (b) PR_{CO} and corresponding FE_{CO} under different applied potentials of all samples. (c) Long-term stability tests and the corresponding FE_{CO} at 1.2 V and 850 °C for NiFe@SFNM and CeO_2–NiFe@SCeFNM. (d) Radar map of SFNM, SCeFNM, NiFe@SFNM and CeO_2–NiFe@SCeFNM. (e) XRD patterns and SEM images of (f) a cross-section of a single cell and (g) CeO_2–NiFe@SCeFNM cathode as well as (h) Raman spectra of the CeO_2–NiFe@SCeFNM cathodes before and after stability testing.

CO_2/CO, as also confirmed by the Raman spectrum of the CeO_2–NiFe@SFNM cathode after stability testing in Fig. 4h. Notably, no obvious peaks associated with $SrCO_3$ (1050 cm^{-1}), D-bond (1340 cm^{-1}) and G-bond (1580 cm^{-1}) were observed, evidencing the good coking resistance and the strong suppression to Sr segregation of CeO_2–NiFe@SCeFNM.[27]

To clearly elaborate the mechanism credited for the superior electrochemical activity on CeO_2–NiFe@SCeFNM, a schematic illustration of the possible reaction pathways over SFNM, NiFe@SFNM and CeO_2–NiFe@SCeFNM is shown in Fig. 5. It was seen that when SFNM was assembled as a cathode, its activity was limited to the slow gas–solid interface exchange process involving CO_2 adsorption, activation, and O^{2-} migration on the cathode surfaces (Fig. 5a). Nevertheless, the introduction of NiFe alloy NPs characterized by high electronic conductivity could promote charge transfer, and CO_2 adsorption and activation in CO_2 electrolysis, but individual NiFe alloy NPs suffered from insufficient O^{2-} migration (Fig. 5b). Thus, we proposed the "three-in-one" strategy in this study by integrating both NiFe alloy NPs and defective CeO_2 phase *in situ* exsolved from SCeFNM (Fig. 5c), which synergistically increased the ionic-electronic conductivity and the O^{2-} migration channels from CeO_2 to SCeFNM to promote CO_2 adsorption and activation. In addition, the intimate contact of

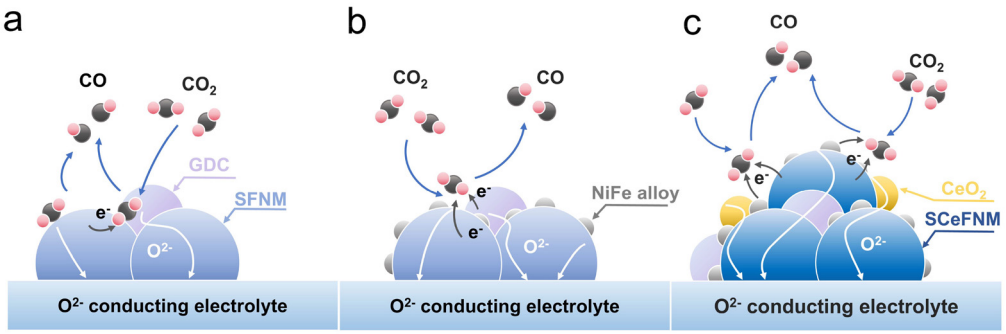

Fig. 5 Schematic illustrations of possible reaction pathways for CO_2 electrolysis over (a) SFNM, (b) NiFe@SFNM and (c) CeO_2–NiFe@SCeFNM.

SCeFNM, NiFe alloy NPs and CeO_2 at the nanoscale also effectively extended the triple-phase boundary length dedicated to CO_2 electrolysis, thus culminating in the exceptional CO_2 electrolysis activity.

4. Conclusions

In summary, we synthesized $Sr_{1.95}Ce_{0.05}Fe_{1.3}Ni_{0.2}Mo_{0.5}O_{6-\delta}$ (SCeFNM) using a Ce-doping strategy, and strategically constructed CeO_2–NiFe/oxide heterostructures by *in situ* co-exsolving oxygen-vacancy-rich CeO_2 phase and NiFe alloy NPs from perovskite oxide (CeO_2–NiFe@SCeFNM) to avoid the co-segregation of insulating SrO phase. It was found that CeO_2–NiFe@SCeFNM cathode achieved a j of 1.57 A cm^{-2} at 850 °C and 1.5 V, and a CO faradaic efficiency of 96%, outperforming NiFe@SFNM without oxygen-deficient CeO_2 phase, and pristine SFNM and SCeFNM. Crucially, the cathode demonstrated an exceptional operational stability over 120 hours without carbon deposition and particle agglomeration, overcoming the degradation limitations of traditional exsolution. Combined results and spectra collectively verified that the enhanced activity exhibited by CeO_2–NiFe@SCeFNM was mainly derived from the three-in-one structure, where the NiFe alloy NPs on CeO_2–NiFe@SCeFNM enhanced the electronic conductivity, and the CeO_2 phase facilitated O^{2-} migration as well as CO_2 adsorption and activation, while the perovskite oxide framework ensured the structural integrity. The strong interaction between the three phases in the nanodomain creates a "win–win" effect, and results in an optimal CO_2 electrolysis activity, which also presents a promising approach to enhancing SOEC performances by dual exsolution of A-site metal oxides and B-site metal NPs from perovskite oxides.

Author contributions

Biao Ouyang: conceptualization, investigation, writing – original draft preparation. Ming Yang: validation, data curation. Lin-Bo Liu: methodology. Shuo Liu: formal analysis. Yan Li: data curation. Xian-Zhu Fu: supervision. Yifei Sun: conceptualization. Subiao Liu: conceptualization, project administration, resources, supervision, writing – review and editing. Jing-Li Luo: supervision, validation.

Conflicts of interest

There are no conflicts of interest to declare.

Data availability

The data supporting this paper have been included as part of the supplementary information (SI). Supplementary information is available. See DOI: https://doi.org/10.1039/d5gc04390e.

Acknowledgements

This work is supported by the Pilot Group Program of the Research Fund for International Senior Scientists (Grant No. 22350710789) and the Start-up Funding of Central South University (No. 206030104). This project was also supported by Shenzhen Science and Technology Program (JCYJ20240813145707010, JCYJ20220530143401002, JCYJ20241202124410015). The authors are grateful for resources from the High-Performance Computing Center of Central South University.

References

1 H. D. Matthews and S. Wynes, *Science*, 2022, **376**, 1404–1409.
2 P. De Luna, C. Hahn, D. Higgins, S. A. Jaffer, T. F. Jaramillo and E. H. Sargent, *Science*, 2019, **364**, eaav3506.
3 X. Hou, Y. Jiang, K. Wei, C. Jiang, T.-C. Jen, Y. Yao, X. Liu, J. Ma and J. T. S. Irvine, *Chem. Rev.*, 2024, **124**, 5119–5166.
4 J.-h. Myung, D. Neagu, D. N. Miller and J. T. S. Irvine, *Nature*, 2016, **537**, 528–531.
5 T. L. Skafte, P. Blennow, J. Hjelm and C. Graves, *J. Power Sources*, 2018, **373**, 54–60.
6 Y. Sun, Z. Liu, W. Zhang, X. Chu, Y. Cong, K. Huang and S. Feng, *Small*, 2019, **15**, 1803513.
7 J. Ni, L. Chen, J. Lin and S. Kawi, *Nano Energy*, 2012, **1**, 674–686.
8 R. Xu, S. Liu, M. Yang, G. Yang, Z. Luo, R. Ran, W. Zhou and Z. Shao, *Chem. Sci.*, 2024, **15**, 11166–11187.
9 M. Yang, L.-B. Liu, S. Liu, Y. Li, B. Ouyang, X.-Z. Fu, J.-L. Luo, Y. Sun and S. Liu, *Chin. Chem. Lett.*, 2024, 110603.
10 Q. A. Islam, S. Paydar, N. Akbar, B. Zhu and Y. Wu, *J. Power Sources*, 2021, **492**, 229626.
11 B.-W. Zhang, M.-N. Zhu, M.-R. Gao, X. Xi, N. Duan, Z. Chen, R.-F. Feng, H. Zeng and J.-L. Luo, *Nat. Commun.*, 2022, **13**, 4618.
12 H. Lv, T. Liu, X. Zhang, Y. Song, H. Matsumoto, N. Ta, C. Zeng, G. Wang and X. Bao, *Angew. Chem., Int. Ed.*, 2020, **59**, 15968–15973.
13 F. He, M. Hou, F. Zhu, D. Liu, H. Zhang, F. Yu, Y. Zhou, Y. Ding, M. Liu and Y. Chen, *Adv. Energy Mater.*, 2022, **12**, 2202175.
14 S. Jo, Y. H. Kim, H. Jeong, C.-h. Park, B.-R. Won, H. Jeon, K. T. Lee and J.-h. Myung, *Appl. Energy*, 2022, **323**, 119615.
15 D. He, W. Ruan, J. Li, J. Ni and C. Ni, *Chem. Eng. J.*, 2022, **433**, 133632.
16 B.-W. Zhang, M.-N. Zhu, M.-R. Gao, J. Chen, X. Xi, J. Shen, R.-F. Feng, N. Semagina, N. Duan, H. Zeng and J.-L. Luo, *Angew. Chem., Int. Ed.*, 2023, **62**, e202305552.
17 B. Koo, K. Kim, J. K. Kim, H. Kwon, J. W. Han and W. Jung, *Joule*, 2018, **2**, 1476–1499.
18 H. Téllez, J. Druce, J. A. Kilner and T. Ishihara, *Faraday Discuss.*, 2015, **182**, 145–157.

19 Y. Tian, Y. Liu, A. Naden, L. Jia, M. Xu, W. Cui, B. Chi, J. Pu, J. T. S. Irvine and J. Li, *J. Mater. Chem. A*, 2020, **8**, 14895–14899.
20 J. Zhu, W. Zhang, Y. Li, W. Yue, G. Geng and B. Yu, *Appl. Catal., B*, 2020, **268**, 118389.
21 E. Wang, C. Jin, L. Zhao, Z. Yang, C. Liu, S. Wang, X. Lei, M. Chao, H. Xu and R. Yang, *Chem. Eng. J.*, 2024, **494**, 153129.
22 Y. Yi, X. Xi, L. Huang, X. Liu, Y. Liao, J. Liu, J. Long, J. Zhang, X.-Z. Fu and J.-L. Luo, *Adv. Funct. Mater.*, 2025, **35**, 2412486.
23 S. Liu, H. Luo, Y. Li, Q. Liu and J.-L. Luo, *Nano Energy*, 2017, **40**, 115–121.
24 L.-B. Liu, Y.-F. Tang, S. Liu, M. Yu, Y. Sun, X.-Z. Fu, J.-L. Luo and S. Liu, *Adv. Energy Mater.*, 2025, **15**, 2402967.
25 S. Liu, L.-B. Liu, M. Yang, Y. Li, Q. Pan, Y. Sun, X.-Z. Fu, S. Liu and J.-L. Luo, *Chem. Eng. J.*, 2025, **519**, 165404.
26 F. Hu, Y. Ling, S. Fang, L. Sui, H. Xiao, Y. Huang, S. Wang, B. He and L. Zhao, *Appl. Catal., B*, 2023, **337**, 122968.
27 Y. Li, Y. Li, Y. Wan, Y. Xie, J. Zhu, H. Pan, X. Zheng and C. Xia, *Adv. Energy Mater.*, 2019, **9**, 1803156.
28 Y. Luo, X. Chang, J. Wang, D. Zhang, L. Fu, X.-K. Gu, Y. Wang, T. Liu and M. Ding, *ACS Nano*, 2025, **19**, 1463–1477.
29 Y. Song, X. Zhang, K. Xie, G. Wang and X. Bao, *Adv. Mater.*, 2019, **31**, 1902033.
30 L. Zhang, C. Xu, W. Sun, R. Ren, X. Yang, Y. Luo, J. Qiao, Z. Wang, S. Zhen and K. Sun, *Sep. Purif. Technol.*, 2022, **298**, 121475.
31 X. Xi, Y. Fan, J. Zhang, J.-L. Luo and X.-Z. Fu, *J. Mater. Chem. A*, 2022, **10**, 2509–2518.
32 L.-B. Liu, S. Liu, M. Yang, Y. Li, B. Ouyang, P. Zhang, X.-Z. Fu, Y. Sun, S. Liu and J.-L. Luo, *Appl. Catal., B*, 2025, **379**, 125705.